Observation of the Ω_b^- baryon and measurement of the properties of the Ξ_b^- and Ω_b^- baryons

T. Aaltonen,[24] J. Adelman,[14] T. Akimoto,[56] B. Álvarez González,[12,u] S. Amerio,[44b,44a] D. Amidei,[35] A. Anastassov,[39] A. Annovi,[20] J. Antos,[15] G. Apollinari,[18] A. Apresyan,[49] T. Arisawa,[58] A. Artikov,[16] W. Ashmanskas,[18] A. Attal,[4] A. Aurisano,[54] F. Azfar,[43] W. Badgett,[18] A. Barbaro-Galtieri,[29] V. E. Barnes,[49] B. A. Barnett,[26] P. Barria,[47c,47a] V. Bartsch,[31] G. Bauer,[33] P.-H. Beauchemin,[34] F. Bedeschi,[47a] D. Beecher,[31] S. Behari,[26] G. Bellettini,[47b,47a] J. Bellinger,[60] D. Benjamin,[17] A. Beretvas,[18] J. Beringer,[29] A. Bhatti,[51] M. Binkley,[18] D. Bisello,[44b,44a] I. Bizjak,[31,z] R. E. Blair,[2] C. Blocker,[7] B. Blumenfeld,[26] A. Bocci,[17] A. Bodek,[50] V. Boisvert,[50] G. Bolla,[49] D. Bortoletto,[49] J. Boudreau,[48] A. Boveia,[11] B. Brau,[11,b] A. Bridgeman,[25] L. Brigliadori,[6b,6a] C. Bromberg,[36] E. Brubaker,[14] J. Budagov,[16] H. S. Budd,[50] S. Budd,[25] S. Burke,[18] K. Burkett,[18] G. Busetto,[44b,44a] P. Bussey,[22] A. Buzatu,[34] K. L. Byrum,[2] S. Cabrera,[17,w] C. Calancha,[32] M. Campanelli,[36] M. Campbell,[35] F. Canelli,[14,18] A. Canepa,[46] B. Carls,[25] D. Carlsmith,[60] R. Carosi,[47a] S. Carrillo,[19,o] S. Carron,[34] B. Casal,[12] M. Casarsa,[18] A. Castro,[6b,6a] P. Catastini,[47c,47a] D. Cauz,[55b,55a] V. Cavaliere,[47c,47a] M. Cavalli-Sforza,[4] A. Cerri,[29] L. Cerrito,[31,q] S. H. Chang,[28] Y. C. Chen,[1] M. Chertok,[8] G. Chiarelli,[47a] G. Chlachidze,[18] F. Chlebana,[18] K. Cho,[28] D. Chokheli,[16] J. P. Chou,[23] G. Choudalakis,[33] S. H. Chuang,[53] K. Chung,[18,p] W. H. Chung,[60] Y. S. Chung,[50] T. Chwalek,[27] C. I. Ciobanu,[45] M. A. Ciocci,[47c,47a] A. Clark,[21] D. Clark,[7] G. Compostella,[44a] M. E. Convery,[18] J. Conway,[8] M. Cordelli,[20] G. Cortiana,[44b,44a] C. A. Cox,[8] D. J. Cox,[8] F. Crescioli,[47b,47a] C. Cuenca Almenar,[8,w] J. Cuevas,[12,u] R. Culbertson,[18] J. C. Cully,[35] D. Dagenhart,[18] M. Datta,[18] T. Davies,[22] P. de Barbaro,[50] S. De Cecco,[52a] A. Deisher,[29] G. De Lorenzo,[4] M. Dell'Orso,[47b,47a] C. Deluca,[4] L. Demortier,[51] J. Deng,[17] M. Deninno,[6a] P. F. Derwent,[18] A. Di Canto,[47b,47a] G. P. di Giovanni,[45] C. Dionisi,[52b,52a] B. Di Ruzza,[55b,55a] J. R. Dittmann,[5] M. D'Onofrio,[4] S. Donati,[47b,47a] P. Dong,[9] J. Donini,[44a] J. Dorigo,[44a] S. Dube,[53] J. Efron,[40] A. Elagin,[54] R. Erbacher,[8] D. Errede,[25] S. Errede,[25] R. Eusebi,[18] H. C. Fang,[29] S. Farrington,[43] W. T. Fedorko,[14] R. G. Feild,[61] M. Feindt,[27] J. P. Fernandez,[32] C. Ferrazza,[47d,47a] R. Field,[19] G. Flanagan,[49] R. Forrest,[8] M. J. Frank,[5] M. Franklin,[23] J. C. Freeman,[18] I. Furic,[19] M. Gallinaro,[52a] J. Galyardt,[13] F. Garberson,[11] J. E. Garcia,[21] A. F. Garfinkel,[49] P. Garosi,[47c,47a] K. Genser,[18] H. Gerberich,[25] D. Gerdes,[35] A. Gessler,[27] S. Giagu,[52b,52a] V. Giakoumopoulou,[3] P. Giannetti,[47a] K. Gibson,[48] J. L. Gimmell,[50] C. M. Ginsburg,[18] N. Giokaris,[3] M. Giordani,[55b,55a] P. Giromini,[20] M. Giunta,[47a] G. Giurgiu,[26] V. Glagolev,[16] D. Glenzinski,[18] M. Gold,[38] N. Goldschmidt,[19] A. Golossanov,[18] G. Gomez,[12] G. Gomez-Ceballos,[33] M. Goncharov,[33] O. González,[32] I. Gorelov,[38] A. T. Goshaw,[17] K. Goulianos,[51] A. Gresele,[44b,44a] S. Grinstein,[23] C. Grosso-Pilcher,[14] R. C. Group,[18] U. Grundler,[25] J. Guimaraes da Costa,[23] Z. Gunay-Unalan,[36] C. Haber,[29] K. Hahn,[33] S. R. Hahn,[18] E. Halkiadakis,[53] B.-Y. Han,[50] J. Y. Han,[50] F. Happacher,[20] K. Hara,[56] D. Hare,[53] M. Hare,[57] S. Harper,[43] R. F. Harr,[59] R. M. Harris,[18] M. Hartz,[48] K. Hatakeyama,[51] C. Hays,[43] M. Heck,[27] A. Heijboer,[46] J. Heinrich,[46] C. Henderson,[33] M. Herndon,[60] J. Heuser,[27] S. Hewamanage,[5] D. Hidas,[17] C. S. Hill,[11,d] D. Hirschbuehl,[27] A. Hocker,[18] S. Hou,[1] M. Houlden,[30] S.-C. Hsu,[29] B. T. Huffman,[43] R. E. Hughes,[40] U. Husemann,[61] M. Hussein,[36] J. Huston,[36] J. Incandela,[11] G. Introzzi,[47a] M. Iori,[52b,52a] A. Ivanov,[8] E. James,[18] D. Jang,[13] B. Jayatilaka,[17] E. J. Jeon,[28] M. K. Jha,[6a] S. Jindariani,[18] W. Johnson,[8] M. Jones,[49] K. K. Joo,[28] S. Y. Jun,[13] J. E. Jung,[28] T. R. Junk,[18] T. Kamon,[54] D. Kar,[19] P. E. Karchin,[59] Y. Kato,[42,n] R. Kephart,[18] W. Ketchum,[14] J. Keung,[46] V. Khotilovich,[54] B. Kilminster,[18] D. H. Kim,[28] H. S. Kim,[28] H. W. Kim,[28] J. E. Kim,[28] M. J. Kim,[20] S. B. Kim,[28] S. H. Kim,[56] Y. K. Kim,[14] N. Kimura,[56] L. Kirsch,[7] S. Klimenko,[19] B. Knuteson,[33] B. R. Ko,[17] K. Kondo,[58] D. J. Kong,[28] J. Konigsberg,[19] A. Korytov,[19] A. V. Kotwal,[17] M. Kreps,[27] J. Kroll,[46] D. Krop,[14] N. Krumnack,[5] M. Kruse,[17] V. Krutelyov,[11] T. Kubo,[56] T. Kuhr,[27] N. P. Kulkarni,[59] M. Kurata,[56] S. Kwang,[14] A. T. Laasanen,[49] S. Lami,[47a] S. Lammel,[18] M. Lancaster,[31] R. L. Lander,[8] K. Lannon,[40,t] A. Lath,[53] G. Latino,[47c,47a] I. Lazzizzera,[44b,44a] T. LeCompte,[2] E. Lee,[54] H. S. Lee,[14] S. W. Lee,[54,v] S. Leone,[47a] J. D. Lewis,[18] C.-S. Lin,[29] J. Linacre,[43] M. Lindgren,[18] E. Lipeles,[46] A. Lister,[8] D. O. Litvintsev,[18] C. Liu,[48] T. Liu,[18] N. S. Lockyer,[46] A. Loginov,[61] M. Loreti,[44b,44a] L. Lovas,[15] D. Lucchesi,[44b,44a] C. Luci,[52b,52a] J. Lueck,[27] P. Lujan,[29] P. Lukens,[18] G. Lungu,[51] L. Lyons,[43] J. Lys,[29] R. Lysak,[15] D. MacQueen,[34] R. Madrak,[18] K. Maeshima,[18] K. Makhoul,[33] T. Maki,[24] P. Maksimovic,[26] S. Malde,[43] S. Malik,[31] G. Manca,[30,f] A. Manousakis-Katsikakis,[3] F. Margaroli,[49] C. Marino,[27] C. P. Marino,[25] A. Martin,[61] V. Martin,[22,l] M. Martínez,[4] R. Martínez-Ballarín,[32] T. Maruyama,[56] P. Mastrandrea,[52a] T. Masubuchi,[56] M. Mathis,[26] M. E. Mattson,[59] P. Mazzanti,[6a] K. S. McFarland,[50] P. McIntyre,[54] R. McNulty,[30,k] A. Mehta,[30] P. Mehtala,[24] A. Menzione,[47a] P. Merkel,[49] C. Mesropian,[51] T. Miao,[18] N. Miladinovic,[7] R. Miller,[36] C. Mills,[23] M. Milnik,[27] A. Mitra,[1] G. Mitselmakher,[19] H. Miyake,[56] N. Moggi,[6a] M. N. Mondragon,[18,o] C. S. Moon,[28] R. Moore,[18] M. J. Morello,[47a] J. Morlock,[27] P. Movilla Fernandez,[18] J. Mülmenstädt,[29] A. Mukherjee,[18] Th. Muller,[27] R. Mumford,[26] P. Murat,[18] M. Mussini,[6b,6a] J. Nachtman,[18,p] Y. Nagai,[56] A. Nagano,[56] J. Naganoma,[56] K. Nakamura,[56] I. Nakano,[41] A. Napier,[57] V. Necula,[17] J. Nett,[60] C. Neu,[46,x] M. S. Neubauer,[25] S. Neubauer,[27]

J. Nielsen,[29,h] L. Nodulman,[2] M. Norman,[10] O. Norniella,[25] E. Nurse,[31] L. Oakes,[43] S. H. Oh,[17] Y. D. Oh,[28] I. Oksuzian,[19] T. Okusawa,[42] R. Orava,[24] K. Osterberg,[24] S. Pagan Griso,[44b,44a] E. Palencia,[18] V. Papadimitriou,[18] A. Papaikonomou,[27] A. A. Paramonov,[14] B. Parks,[40] S. Pashapour,[34] J. Patrick,[18] G. Pauletta,[55b,55a] M. Paulini,[13] C. Paus,[33] T. Peiffer,[27] D. E. Pellett,[8] A. Penzo,[55a] T. J. Phillips,[17] G. Piacentino,[47a] E. Pianori,[46] L. Pinera,[19] K. Pitts,[25] C. Plager,[9] L. Pondrom,[60] O. Poukhov,[16,a] N. Pounder,[43] F. Prakoshyn,[16] A. Pronko,[18] J. Proudfoot,[2] F. Ptohos,[18,j] E. Pueschel,[13] G. Punzi,[47b,47a] J. Pursley,[60] J. Rademacker,[43,d] A. Rahaman,[48] V. Ramakrishnan,[60] N. Ranjan,[49] I. Redondo,[32] P. Renton,[43] M. Renz,[27] M. Rescigno,[52a] S. Richter,[27] F. Rimondi,[6b,6a] L. Ristori,[47a] A. Robson,[22] T. Rodrigo,[12] T. Rodriguez,[46] E. Rogers,[25] S. Rolli,[57] R. Roser,[18] M. Rossi,[55a] R. Rossin,[11] P. Roy,[34] A. Ruiz,[12] J. Russ,[13] V. Rusu,[18] B. Rutherford,[18] H. Saarikko,[24] A. Safonov,[54] W. K. Sakumoto,[50] O. Saltó,[4] L. Santi,[55b,55a] S. Sarkar,[52b,52a] L. Sartori,[47a] K. Sato,[18] A. Savoy-Navarro,[45] P. Schlabach,[18] A. Schmidt,[27] E. E. Schmidt,[18] M. A. Schmidt,[14] M. P. Schmidt,[61,a] M. Schmitt,[39] T. Schwarz,[8] L. Scodellaro,[12] A. Scribano,[47c,47a] F. Scuri,[47a] A. Sedov,[49] S. Seidel,[38] Y. Seiya,[42] A. Semenov,[16] L. Sexton-Kennedy,[18] F. Sforza,[47b,47a] A. Sfyrla,[25] S. Z. Shalhout,[59] T. Shears,[30] P. F. Shepard,[48] M. Shimojima,[56,b] S. Shiraishi,[14] M. Shochet,[14] Y. Shon,[60] I. Shreyber,[37] P. Sinervo,[34] A. Sisakyan,[16] A. J. Slaughter,[18] J. Slaunwhite,[40] K. Sliwa,[57] J. R. Smith,[8] F. D. Snider,[18] R. Snihur,[34] A. Soha,[8] S. Somalwar,[53] V. Sorin,[36] T. Spreitzer,[34] P. Squillacioti,[47c,47a] M. Stanitzki,[61] R. St. Denis,[22] B. Stelzer,[34] O. Stelzer-Chilton,[34] D. Stentz,[39] J. Strologas,[38] G. L. Strycker,[35] J. S. Suh,[28] A. Sukhanov,[19] I. Suslov,[16] T. Suzuki,[56] A. Taffard,[25,g] R. Takashima,[41] Y. Takeuchi,[56] R. Tanaka,[41] M. Tecchio,[35] P. K. Teng,[1] K. Terashi,[51] R. Tesarek,[18] J. Thom,[18,i] A. S. Thompson,[22] G. A. Thompson,[25] E. Thomson,[46] P. Tipton,[61] P. Ttito-Guzmán,[32] S. Tkaczyk,[18] D. Toback,[54] S. Tokar,[15] K. Tollefson,[36] T. Tomura,[56] D. Tonelli,[18] S. Torre,[20] D. Torretta,[18] P. Totaro,[55b,55a] S. Tourneur,[45] M. Trovato,[47d,47a] S.-Y. Tsai,[1] Y. Tu,[46] N. Turini,[47c,47a] F. Ukegawa,[56] S. Vallecorsa,[21] N. van Remortel,[24,c] A. Varganov,[35] E. Vataga,[47d,47a] F. Vázquez,[19,o] G. Velev,[18] C. Vellidis,[3] M. Vidal,[32] R. Vidal,[18] I. Vila,[12] R. Vilar,[12] T. Vine,[31] M. Vogel,[38] I. Volobouev,[29,v] G. Volpi,[47b,47a] P. Wagner,[46] R. G. Wagner,[2] R. L. Wagner,[18] W. Wagner,[27,y] J. Wagner-Kuhr,[27] T. Wakisaka,[42] R. Wallny,[9] S. M. Wang,[1] A. Warburton,[34] D. Waters,[31] M. Weinberger,[54] J. Weinelt,[27] W. C. Wester III,[18] B. Whitehouse,[57] D. Whiteson,[46,g] A. B. Wicklund,[2] E. Wicklund,[18] S. Wilbur,[14] G. Williams,[34] H. H. Williams,[46] P. Wilson,[18] B. L. Winer,[40] P. Wittich,[18,i] S. Wolbers,[18] C. Wolfe,[14] T. Wright,[35] X. Wu,[21] F. Würthwein,[10] S. Xie,[33] A. Yagil,[10] K. Yamamoto,[42] J. Yamaoka,[17] U. K. Yang,[14,r] Y. C. Yang,[28] W. M. Yao,[29] G. P. Yeh,[18] K. Yi,[18,p] J. Yoh,[18] K. Yorita,[58] T. Yoshida,[42,m] G. B. Yu,[50] I. Yu,[28] S. S. Yu,[18] J. C. Yun,[18] L. Zanello,[52b,52a] A. Zanetti,[55a] X. Zhang,[25] Y. Zheng,[9,e] and S. Zucchelli[6a]

(CDF Collaboration)

[1]*Institute of Physics, Academia Sinica, Taipei, Taiwan 11529, Republic of China*
[2]*Argonne National Laboratory, Argonne, Illinois 60439, USA*
[3]*University of Athens, 157 71 Athens, Greece*
[4]*Institut de Fisica d'Altes Energies, Universitat Autonoma de Barcelona, E-08193, Bellaterra (Barcelona), Spain*
[5]*Baylor University, Waco, Texas 76798, USA*
[6a]*Istituto Nazionale di Fisica Nucleare Bologna, I-40127 Bologna, Italy*
[6b]*University of Bologna, I-40127 Bologna, Italy*
[7]*Brandeis University, Waltham, Massachusetts 02254, USA*
[8]*University of California, Davis, Davis, California 95616, USA*
[9]*University of California, Los Angeles, Los Angeles, California 90024, USA*
[10]*University of California, San Diego, La Jolla, California 92093, USA*
[11]*University of California, Santa Barbara, Santa Barbara, California 93106, USA*
[12]*Instituto de Fisica de Cantabria, CSIC-University of Cantabria, 39005 Santander, Spain*
[13]*Carnegie Mellon University, Pittsburgh, Pennsylvania 15213, USA*
[14]*Enrico Fermi Institute, University of Chicago, Chicago, Illinois 60637, USA*
[15]*Comenius University, 842 48 Bratislava, Slovakia;*
Institute of Experimental Physics, 040 01 Kosice, Slovakia
[16]*Joint Institute for Nuclear Research, RU-141980 Dubna, Russia*
[17]*Duke University, Durham, North Carolina 27708, USA*
[18]*Fermi National Accelerator Laboratory, Batavia, Illinois 60510, USA*
[19]*University of Florida, Gainesville, Florida 32611, USA*
[20]*Laboratori Nazionali di Frascati, Istituto Nazionale di Fisica Nucleare, I-00044 Frascati, Italy*
[21]*University of Geneva, CH-1211 Geneva 4, Switzerland*
[22]*Glasgow University, Glasgow G12 8QQ, United Kingdom*
[23]*Harvard University, Cambridge, Massachusetts 02138, USA*

[24]*Division of High Energy Physics, Department of Physics, University of Helsinki and Helsinki Institute of Physics, FIN-00014, Helsinki, Finland*
[25]*University of Illinois, Urbana, Illinois 61801, USA*
[26]*The Johns Hopkins University, Baltimore, Maryland 21218, USA*
[27]*Institut für Experimentelle Kernphysik, Universität Karlsruhe, 76128 Karlsruhe, Germany*
[28]*Center for High Energy Physics: Kyungpook National University, Daegu 702-701, Korea;*
Seoul National University, Seoul 151-742, Korea;
Sungkyunkwan University, Suwon 440-746, Korea;
Korea Institute of Science and Technology Information, Daejeon, 305-806, Korea;
Chonnam National University, Gwangju, 500-757, Korea
[29]*Ernest Orlando Lawrence Berkeley National Laboratory, Berkeley, California 94720, USA*
[30]*University of Liverpool, Liverpool L69 7ZE, United Kingdom*
[31]*University College London, London WC1E 6BT, United Kingdom*
[32]*Centro de Investigaciones Energeticas Medioambientales y Tecnologicas, E-28040 Madrid, Spain*
[33]*Massachusetts Institute of Technology, Cambridge, Massachusetts 02139, USA*
[34]*Institute of Particle Physics: McGill University, Montréal, Québec, Canada H3A 2T8;*
Simon Fraser University, Burnaby, British Columbia, Canada V5A 1S6;
University of Toronto, Toronto, Ontario, Canada M5S 1A7;
and TRIUMF, Vancouver, British Columbia, Canada V6T 2A3
[35]*University of Michigan, Ann Arbor, Michigan 48109, USA*
[36]*Michigan State University, East Lansing, Michigan 48824, USA*
[37]*Institution for Theoretical and Experimental Physics, ITEP, Moscow 117259, Russia*
[38]*University of New Mexico, Albuquerque, New Mexico 87131, USA*
[39]*Northwestern University, Evanston, Illinois 60208, USA*
[40]*The Ohio State University, Columbus, Ohio 43210, USA*
[41]*Okayama University, Okayama 700-8530, Japan*
[42]*Osaka City University, Osaka 588, Japan*
[43]*University of Oxford, Oxford OX1 3RH, United Kingdom*
[44a]*Istituto Nazionale di Fisica Nucleare, Sezione di Padova-Trento, I-35131 Padova, Italy*
[44b]*University of Padova, I-35131 Padova, Italy*
[45]*LPNHE, Universite Pierre et Marie Curie/IN2P3-CNRS, UMR7585, Paris, F-75252 France*
[46]*University of Pennsylvania, Philadelphia, Pennsylvania 19104, USA*
[47a]*Istituto Nazionale di Fisica Nucleare Pisa, I-56127 Pisa, Italy*
[47b]*University of Pisa, I-56127 Pisa, Italy*
[47c]*University of Siena, I-56127 Pisa, Italy*

---

[a]Deceased.

[b]Visitor from University of Massachusetts Amherst, Amherst, MA 01003, USA.

[c]Visitor from Universiteit Antwerpen, B-2610 Antwerp, Belgium.

[d]Visitor from University of Bristol, Bristol BS8 1TL, United Kingdom.

[e]Visitor from Chinese Academy of Sciences, Beijing 100864, China.

[f]Visitor from Istituto Nazionale di Fisica Nucleare, Sezione di Cagliari, 09042 Monserrato (Cagliari), Italy.

[g]Visitor from University of California Irvine, Irvine, CA 92697, USA.

[h]Visitor from University of California Santa Cruz, Santa Cruz, CA 95064, USA.

[i]Visitor from Cornell University, Ithaca, NY 14853, USA.

[j]Visitor from University of Cyprus, Nicosia CY-1678, Cyprus.

[k]Visitor from University College Dublin, Dublin 4, Ireland.

[l]Visitor from University of Edinburgh, Edinburgh EH9 3JZ, United Kingdom.

[m]Visitor from University of Fukui, Fukui City, Fukui Prefecture, Japan 910-0017.

[n]Visitor from Kinki University, Higashi-Osaka City, Japan 577-8502.

[o]Visitor from Universidad Iberoamericana, Mexico D.F., Mexico.

[p]Visitor from University of Iowa, Iowa City, IA 52242, USA.

[q]Visitor from Queen Mary, University of London, London, E1 4NS, England.

[r]Visitor from University of Manchester, Manchester M13 9PL, England.

[s]Visitor from Nagasaki Institute of Applied Science, Nagasaki, Japan.

[t]Visitor from University of Notre Dame, Notre Dame, IN 46556, USA.

[u]University de Oviedo, E-33007 Oviedo, Spain.

[v]Visitor from Texas Tech University, Lubbock, TX 79609, USA.

[w]Visitor from IFIC (CSIC-Universitat de Valencia), 46071 Valencia, Spain.

[x]Visitor from University of Virginia, Charlottesville, VA 22904, USA.

[y]Visitor from Bergische Universität Wuppertal, 42097 Wuppertal, Germany.

[z]On leave from J. Stefan Institute, Ljubljana, Slovenia.

[47d]*Scuola Normale Superiore, I-56127 Pisa, Italy*
[48]*University of Pittsburgh, Pittsburgh, Pennsylvania 15260, USA*
[49]*Purdue University, West Lafayette, Indiana 47907, USA*
[50]*University of Rochester, Rochester, New York 14627, USA*
[51]*The Rockefeller University, New York, New York 10021, USA*
[52a]*Istituto Nazionale di Fisica Nucleare, Sezione di Roma 1, I-00185 Roma, Italy*
[52b]*Sapienza Università di Roma, I-00185 Roma, Italy*
[53]*Rutgers University, Piscataway, New Jersey 08855, USA*
[54]*Texas A&M University, College Station, Texas 77843, USA*
[55a]*Istituto Nazionale di Fisica Nucleare Trieste/Udine, I-34100 Trieste, I-33100 Udine, Italy*
[55b]*University of Trieste/Udine, I-33100 Udine, Italy*
[56]*University of Tsukuba, Tsukuba, Ibaraki 305, Japan*
[57]*Tufts University, Medford, Massachusetts 02155, USA*
[58]*Waseda University, Tokyo 169, Japan*
[59]*Wayne State University, Detroit, Michigan 48201, USA*
[60]*University of Wisconsin, Madison, Wisconsin 53706, USA*
[61]*Yale University, New Haven, Connecticut 06520, USA*

We report the observation of the bottom, doubly-strange baryon Ω_b^- through the decay chain $\Omega_b^- \to J/\psi \Omega^-$, where $J/\psi \to \mu^+\mu^-$, $\Omega^- \to \Lambda K^-$, and $\Lambda \to p\pi^-$, using 4.2 fb^{-1} of data from $p\bar{p}$ collisions at $\sqrt{s} = 1.96$ TeV, and recorded with the Collider Detector at Fermilab. A signal is observed whose probability of arising from a background fluctuation is 4.0×10^{-8}, or 5.5 Gaussian standard deviations. The Ω_b^- mass is measured to be $6054.4 \pm 6.8(\text{stat}) \pm 0.9(\text{syst})$ MeV/c^2. The lifetime of the Ω_b^- baryon is measured to be $1.13^{+0.53}_{-0.40}(\text{stat}) \pm 0.02(\text{syst})$ ps. In addition, for the Ξ_b^- baryon we measure a mass of $5790.9 \pm 2.6(\text{stat}) \pm 0.8(\text{syst})$ MeV/c^2 and a lifetime of $1.56^{+0.27}_{-0.25}(\text{stat}) \pm 0.02(\text{syst})$ ps. Under the assumption that the Ξ_b^- and Ω_b^- are produced with similar kinematic distributions to the Λ_b^0 baryon, we find $\frac{\sigma(\Xi_b^-)\mathcal{B}(\Xi_b^- \to J/\psi \Xi^-)}{\sigma(\Lambda_b^0)\mathcal{B}(\Lambda_b^0 \to J/\psi \Lambda)} = 0.167^{+0.037}_{-0.025}(\text{stat}) \pm 0.012(\text{syst})$ and $\frac{\sigma(\Omega_b^-)\mathcal{B}(\Omega_b^- \to J/\psi \Omega^-)}{\sigma(\Lambda_b^0)\mathcal{B}(\Lambda_b^0 \to J/\psi \Lambda)} = 0.045^{+0.017}_{-0.012}(\text{stat}) \pm 0.004(\text{syst})$ for baryons produced with transverse momentum in the range of 6–20 GeV/c.

I. INTRODUCTION

Since its inception, the quark model has had great success in describing the spectroscopy of hadrons. In particular, this has been the case for the D and B mesons, where all of the ground states have been observed [1]. The spectroscopy of c baryons also agrees well with the quark model, and a rich spectrum of baryons containing b quarks is predicted [2]. Until recently, direct observation of b baryons has been limited to a single state, the Λ_b^0 (quark content $|udb\rangle$) [1]. The accumulation of large data sets from the Tevatron has changed this situation, and made possible the observation of the Ξ_b^- ($|dsb\rangle$) [3,4] and the $\Sigma_b^{(*)}$ states ($|uub\rangle$, $|ddb\rangle$) [5].

In this paper, we report the observation of an additional heavy baryon and the measurement of its mass, lifetime, and relative production rate compared to the Λ_b^0 production. The decay properties of this state are consistent with the weak decay of a b baryon. We interpret our result as the observation of the Ω_b^- baryon ($|ssb\rangle$). Observation of this baryon has been previously reported by the D0 Collaboration [6]. However, the analysis presented here measures a mass of the Ω_b^- to be significantly lower than Ref. [6].

This Ω_b^- observation is made in $p\bar{p}$ collisions at a center of mass energy of 1.96 TeV using the Collider Detector at

Fermilab (CDF II), through the decay chain $\Omega_b^- \to J/\psi \Omega^-$, where $J/\psi \to \mu^+\mu^-$, $\Omega^- \to \Lambda K^-$, and $\Lambda \to p\pi^-$. Charge conjugate modes are included implicitly. Mass, lifetime, and production rate measurements are also reported for the Ξ_b^-, through the similar decay chain $\Xi_b^- \to J/\psi \Xi^-$, where $J/\psi \to \mu^+\mu^-$, $\Xi^- \to \Lambda \pi^-$, and $\Lambda \to p\pi^-$. The production rates of both the Ξ_b^- and Ω_b^- are measured with respect to the Λ_b^0, which is observed through the decay chain $\Lambda_b^0 \to J/\psi \Lambda$, where $J/\psi \to \mu^+\mu^-$, and $\Lambda \to p\pi^-$. These measurements are based on a data sample corresponding to an integrated luminosity of 4.2 fb^{-1}.

The strategy of the analysis presented here is to demonstrate the reconstruction and property measurements of the Ξ_b^- and Ω_b^- as natural extensions of measurements that can be made on better known b hadron states obtained in the same data. All measurements made here are performed on the $B^0 \to J/\psi K^*(892)^0$, $K^*(892)^0 \to K^+\pi^-$ final state, to provide a large sample for comparison to other measurements. The decay mode $B^0 \to J/\psi K_s^0$, $K_s^0 \to \pi^+\pi^-$ is a second reference process. The K_s^0 is reconstructed from tracks that are significantly displaced from the collision, similar to the final state tracks of the Ξ_b^- and Ω_b^-. Although its properties are less well measured than those of the B^0, the $\Lambda_b^0 \to J/\psi \Lambda$ contributes another cross-check of this analysis, since it is a previously measured

state that contains a Λ in its decay chain. The Λ_b^0 also provides the best state for comparison of relative production rates, since it is the largest sample of reconstructed b baryons.

We begin with a brief description of the detector and its simulation in Sec. II. In Sec. III, the reconstruction of J/ψ, neutral K, hyperons, and b hadrons is described. Section IV discusses the extraction and significance of the Ω_b^- signal. In Sec. V, we present measurements of the properties of the Ξ_b^- and Ω_b^-, which include particle masses, lifetimes, and production rates. We conclude in Sec. VI.

II. DETECTOR DESCRIPTION AND SIMULATION

The CDF II detector has been described in detail elsewhere [7]. This analysis primarily relies upon the tracking and muon identification systems. The tracking system consists of four different detector subsystems that operate inside a 1.4 T solenoid. The first of these is a single layer of silicon detectors (L00) at a radius of 1.35–1.6 cm from the axis of the solenoid. It measures track position in the transverse view with respect to the beam, which travels along the z direction. A five-layer silicon detector (SVX II) surrounding L00 measures track positions at radii of 2.5 to 10.6 cm. Each of these layers provides a transverse measurement and a stereo measurement of 90° (three layers) or $\pm 1.2°$ (two layers) with respect to the beam direction. The outermost silicon detector lies between 19 and 30 cm radially, and provides one- or two-track position measurements, depending on the track pseudorapidity (η), where $\eta \equiv -\ln(\tan(\theta/2))$, with θ being the angle between the particle momentum and the proton beam direction. An open-cell drift chamber (COT) completes the tracking system, and covers the radial region from 43 to 132 cm. The COT consists of 96 sense-wire layers, arranged in 8 superlayers of 12 wires each. Four of these superlayers provide axial measurements and four provide stereo views of $\pm 2°$.

Electromagnetic and hadronic calorimeters surround the solenoid coil. Muon candidates from the decay $J/\psi \rightarrow \mu^+ \mu^-$ are identified by two sets of drift chambers located radially outside the calorimeters. The central muon chambers cover the pseudorapidity region $|\eta| < 0.6$, and detect muons with transverse momentum $p_T > 1.4$ GeV/c, where the transverse momentum p_T is defined as the component of the particle momentum perpendicular to the proton beam direction. A second muon system covers the region $0.6 < |\eta| < 1.0$ and detects muons with $p_T > 2.0$ GeV/c. Muon selection is based on matching these measurements to COT tracks, both in projected position and angle. The analysis presented here is based on events recorded with a trigger that is dedicated to the collection of a $J/\psi \rightarrow \mu^+ \mu^-$ sample. The first level of the three-level trigger system requires two muon candidates with matching tracks in the COT and muon chamber systems. The second level imposes the requirement that muon candidates have opposite charge and limits the accepted range of the opening angle. The highest level of the J/ψ trigger reconstructs the muon pair in software, and requires that the invariant mass of the pair falls within the range 2.7–4.0 GeV/c^2.

The mass resolution and acceptance for the b hadrons used in this analysis are studied with a Monte Carlo simulation that generates b quarks according to a next-to-leading-order calculation [8], and produces events containing final state hadrons by simulating b quark fragmentation [9]. The final state decay processes are simulated with the EVTGEN [10] decay program, a value of 6.12 GeV/c^2 is taken for the Ω_b^- mass, and all simulated b hadrons are produced without polarization. The generated events are inputted to the detector and trigger simulation based on a GEANT3 description [11] and processed through the same reconstruction and analysis algorithms that are used for the data.

III. PARTICLE RECONSTRUCTION METHODS

This analysis combines the trajectories of charged particles to infer the presence of several different parent hadrons. These hadrons are distinguished by their lifetimes, due to their weak decay. Consequently, it is useful to define two quantities that are used frequently throughout the analysis which relate the path of weakly decaying objects to their points of origin. Both quantities are defined in the transverse view, and make use of the point of closest approach, $\vec{r}_c$, of the particle trajectory to a point of origin, and the measured particle decay position, $\vec{r}_d$. The first quantity used here is transverse flight distance $f(h)$, of hadron h, which is the distance a particle has traveled in the transverse view. For neutral objects, flight distance is given by $f(h) \equiv (\vec{r}_d - \vec{r}_c) \cdot \vec{p}_T(h)/|\vec{p}_T(h)|$, where $\vec{p}_T(h)$ is the transverse momentum of the hadron candidate. For charged objects, the flight distance is calculated as the arc length in the transverse view from $\vec{r}_c$ to $\vec{r}_d$. A complementary quantity used in this analysis is transverse impact distance $d(h)$, which is the distance of the point of closest approach to the point of origin. For neutral particles, transverse impact distance is given by $d(h) \equiv |(\vec{r}_d - \vec{r}_c) \times \vec{p}_T(h)|/|\vec{p}_T(h)|$. The impact distance of charged particles is simply the distance from $\vec{r}_c$ to the point of origin. The measurement uncertainty on impact distance, $\sigma_{d(h)}$, is calculated from the track parameter uncertainties and the uncertainty on the point of origin.

Several different selection criteria are employed in this analysis to identify the particles used in b hadron reconstruction. These criteria are based on the resolution or acceptance of the CDF detector. No optimization procedure has been used to determine the exact value of any selection requirement, since the analysis spans several final states and comparisons between optimized selection requirements would necessarily be model dependent.
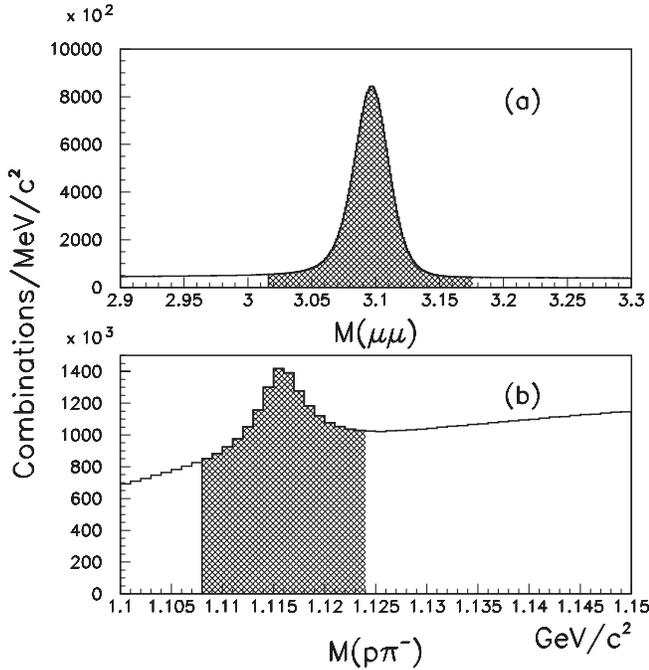
FIG. 1. (a) The $\mu^+\mu^-$ mass distribution obtained in an integrated luminosity of 4.2 fb^{-1}. The mass range used for the J/ψ sample is indicated by the shaded area. (b) The $p\pi^-$ mass distribution obtained in events containing J/ψ candidates. The mass range used for the Λ sample is indicated by the shaded area.

A. J/ψ Reconstruction

The analysis of the data begins with a selection of well-measured $J/\psi \rightarrow \mu^+\mu^-$ candidates. The trigger requirements are confirmed by selecting events that contain two oppositely charged muon candidates, each with matching COT and muon chamber tracks. Both muon tracks are required to have associated position measurements in at least three layers of the SVX II and a two-track invariant mass within 80 MeV/c^2 of the world-average J/ψ mass [1]. This range was chosen for consistency with our earlier b hadron mass measurements [12]. The $\mu^+\mu^-$ mass distribution obtained in these data is shown in Fig. 1(a). This data sample provides approximately 2.9×10^7 J/ψ candidates, measured with an average mass resolution of ~ 20 MeV/c^2.

B. Neutral hadron reconstruction

The reconstruction of K_s^0, $K^*(892)^0$, and Λ candidates uses all tracks with $p_T > 0.4$ GeV/c found in the COT, that are not associated with muons in the J/ψ reconstruction. Pairs of oppositely charged tracks are combined to identify these neutral decay candidates, and silicon detector information is not used. Candidate selection for these neutral states is based upon the mass calculated for each track pair, which is required to fall within the ranges given in Table I after the appropriate mass assignment for each track.

TABLE I. Mass ranges around the nominal mass value [1] used for the b hadron decay products.

Resonance (final state)	Mass range (MeV/c^2)
$J/\psi(\mu^+\mu^-)$	± 80
$K^*(892)^0(K^+\pi^-)$	± 30
$K_s^0(\pi^+\pi^-)$	± 20
$\Lambda(p\pi^-)$	± 9
$\Xi^-(\Lambda\pi^-)$	± 9
$\Omega^-(\Lambda K^-)$	± 8

Candidates for K_s^0 decay are chosen by assigning the pion mass to each track, and mass is measured with a resolution of ~ 6 MeV/c^2. Track pairs used for $K^*(892)^0 \rightarrow K^+\pi^-$ candidates have both mass assignments examined. A broad mass selection range is chosen for the $K^*(892)^0$ signal, due to its natural width of 50 MeV/c^2 [1]. In the situation where both assignments fall within our selection mass range, only the combination closest to the nominal $K^*(892)^0$ mass is used. For $\Lambda \rightarrow p\pi^-$ candidates, the proton (pion) mass is assigned to the track with the higher (lower) momentum. This mass assignment is always correct for the Λ candidates used in this analysis because of the kinematics of Λ decay and the lower limit in the transverse momentum acceptance of the tracking system. Backgrounds to the K_s^0 ($c\tau =$ 2.7 cm) and Λ ($c\tau = 7.9$ cm) [1] are reduced by requiring the flight distance of the K_s^0 and Λ with respect to the primary vertex (defined as the beam position in the transverse view) to be greater than 1.0 cm, which corresponds to $\sim 0.6\sigma$. The mass distribution of the $p\pi^-$ combinations with $p_T(\Lambda) > 2.0$ GeV/c is plotted in Fig. 1(b), and contains approximately 3.6×10^6 Λ candidates.

C. Charged hyperon reconstruction

For events that contain a Λ candidate, the remaining tracks reconstructed in the COT, again without additional silicon information, are assigned the pion or kaon mass, and $\Lambda\pi^-$ or ΛK^- combinations are identified that are consistent with the decay process $\Xi^- \rightarrow \Lambda\pi^-$ or $\Omega^- \rightarrow \Lambda K^-$. Analysis of the simulated Ξ_b^- events shows that the p_T distribution of the π^- daughters of reconstructed Λ and Ξ^- decays falls steeply with increasing $p_T(\pi^-)$. Consequently, tracks with p_T as low as 0.4 GeV/c are used for these reconstructions. The simulation also indicates that the p_T distribution of the K^- daughters from Ω^- decay has a higher average value, and declines with p_T much more slowly than the p_T distribution of the pions from Λ or Ξ^- decays. A study of the ΛK^- combinatorial backgrounds in two 8 MeV/c^2 mass ranges and centered ± 20 MeV/c^2 from the Ω^- mass indicates that the background track p_T distribution is also steeper than the expected distribution of K^- from Ω^- decay. Therefore, $p_T(K^-) > 1.0$ GeV/c is required for our Ω^- sample, which reduces the combinatorial background by 60%,
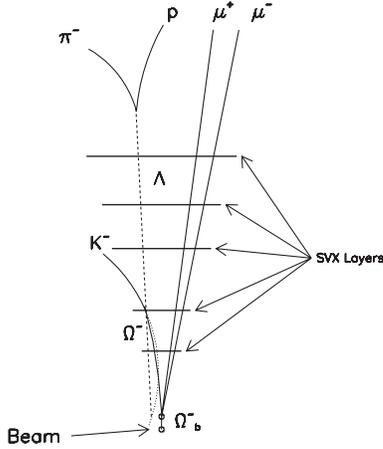
FIG. 2.   An illustration (not to scale) of the $\Omega_b^- \to J/\psi \Omega^-$, $J/\psi \to \mu^+ \mu^-$, $\Omega^- \to \Lambda K^-$, and $\Lambda \to p \pi^-$ final states as seen in the view transverse to the beam direction. Five charged tracks are used to identify three decay vertices. The final fit of these track trajectories constrains the decay hadrons (J/ψ, Ω^-, and Λ) to their nominal masses and the helix of the Ω^- to originate from the J/ψ decay vertex. The trajectory of the K^- is projected back, indicated by a dotted curve, to illustrate how an alternative, incorrect intersection with the Λ trajectory could exist. A comparison of the fit quality of the two ΛK^- intersections is used to choose a preferred solution.

while reducing the Ω^- signal predicted by our Monte Carlo simulation by 25%.

An illustration of the full Ω_b^- final state that is reconstructed in this analysis is shown in Fig. 2. Several features of the track topology are used to reduce the background to this process. In order to obtain the best possible mass resolution for Ξ^- and Ω^- candidates, the reconstruction requires a convergent fit of the three tracks that simultaneously constrains the Λ decay products to the Λ mass, and the Λ trajectory to intersect with the helix of the $\pi^-(K^-)$ originating from the $\Xi^-(\Omega^-)$ candidate. In addition, the flight distance of the Λ candidate with respect to the reconstructed decay vertex of the $\Xi^-(\Omega^-)$ candidate is required to exceed 1.0 cm. Similarly, due to the long lifetimes of the Ξ^- ($c\tau = 4.9$ cm) and Ω^- ($c\tau = 2.5$ cm) [1], a flight distance of at least 1.0 cm (corresponding to $\sim 1.0\sigma$) with respect to the primary vertex is required. This requirement removes $\sim 75\%$ of the background to these long-lived particles, due to prompt particle production.

Possible kinematic reflections are removed from the Ω^- sample by requiring that the combinations in the sample fall outside the Ξ^- mass range listed in Table I when the candidate K^- track is assigned the mass of the π^-. In some instances, the rotation of the $\pi^-(K^-)$ helix produces a situation where two $\Lambda\pi^-(\Lambda K^-)$ vertices satisfy the constrained fit and displacement requirements. These situations are resolved with the tracking measurements in the longitudinal view. The candidate with the poorer value of

probability $P(\chi^2)$ for the $\Xi^-(\Omega^-)$ fit is dropped from the sample. An example of such a combination is illustrated in Fig. 2. The complexity of the $\Xi^-(\Omega^-)$ and Λ decays allows for occasional combinations where the proper identity of the three tracks is ambiguous. An example is where the $\pi^-(K^-)$ candidate track and the π^- candidate track from Λ decay are interchanged, and the interchanged solution satisfies the various mass and flight distance requirements. A single, preferred candidate is chosen by retaining only the fit combination with the highest $P(\chi^2)$ of all the possibilities. Requiring the impact distance with respect to the primary vertex to be less than $3\sigma_{d(h)}$ and $p_T(h) > 2.0$ GeV/c results in the combinations shown in the $\Lambda\pi^-$ and ΛK^- mass distributions of Fig. 3. Approximately 41 000 Ξ^- and 3500 Ω^- candidates are found in this data sample.

The mass distributions in Fig. 3 show clear Ξ^- and Ω^- signals. However, the Ω^- signal has a substantially larger combinatorial background. The kinematics of hyperon decay and the lower p_T limit of 0.4 GeV/c on the decay daughter tracks force the majority of charged hyperon candidates to have $p_T > 1.5$ GeV/c. This fact, along with the long lifetimes of the Ξ^- and Ω^-, results in a significant fraction of the hyperon candidates having decay vertices located several centimeters radially outward from the beam position. Therefore, we are able to refine the charged hyperon reconstruction by making use of the
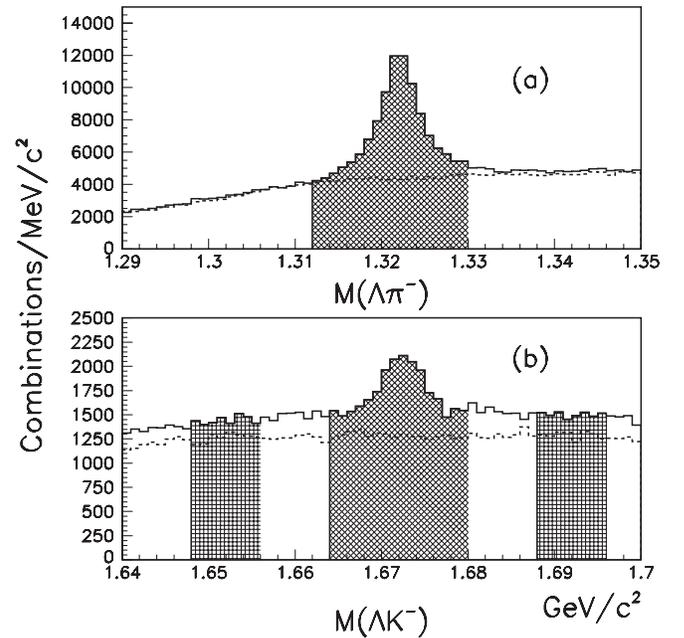

FIG. 3.   The invariant mass distributions of (a) $\Lambda\pi^-$ combinations and (b) ΛK^- combinations in events containing J/ψ candidates. Shaded areas indicate the mass ranges used for Ξ^- and Ω^- candidates. The dashed histograms in each distribution correspond to $\Lambda\pi^+$ (a) and ΛK^+ (b) combinations. Additional shading in (b) correspond to sideband regions discussed in Sec. IV.

improved determination of the trajectory that can be obtained by tracking these particles in the silicon detector. The charged hyperon candidates have an additional fit performed with the three tracks that simultaneously constrains both the Λ and Ξ^- or Ω^- masses of the appropriate track combinations, and provides the best possible estimate of the hyperon momentum and decay position. The result of this fit is used to define a helix that serves as the seed for an algorithm that associates silicon detector hits with the charged hyperon track. Charged hyperon candidates with track measurements in at least one layer of the silicon detector have excellent impact distance resolution (average of 60 μm) for the charged hyperon track. The mass distributions for the subset of the inclusive $\Lambda\pi^-$ and ΛK^- combinations which are found in the silicon detector, and have an impact distance with respect to the primary vertex $d(h) < 3\sigma_{d(h)}$ are shown in Fig. 4. This selection provides approximately 34 700 Ξ^- candidates and 1900 Ω^- candidates with very low combinatorial background, which allows us to confirm the mass resolutions used to select hyperons. Unfortunately, the shorter lifetime of the Ω^- makes the silicon selection less efficient than it is for the Ξ^-. Therefore, silicon detector information on the hyperon track is used whenever it is available, but is not imposed as a requirement for the Ω^- selection.
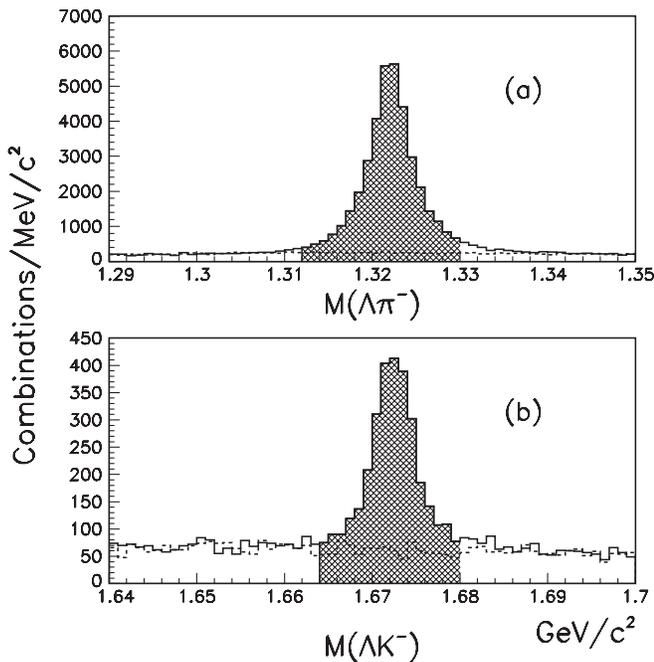

FIG. 4.   The invariant mass distributions of (a) $\Lambda\pi^-$ combinations and (b) ΛK^- combinations in events containing J/ψ candidates. These combinations require silicon information to be used on the hyperon track and the impact distance with respect to the primary vertex must not exceed 3 times its measurement resolution. Shaded areas indicate the mass ranges used for Ξ^- and Ω^- candidates. The dashed histograms in each distribution correspond to $\Lambda\pi^+$ and ΛK^+ combinations.

D. *b* hadron reconstruction

The reconstruction of *b* hadron candidates uses the same method for each of the states reconstructed for this analysis. The *K* and hyperon candidates are combined with the J/ψ candidates by fitting the full four-track or five-track state with constraints appropriate for each decay topology and intermediate hadron state. Specifically, the $\mu^+\mu^-$ mass is constrained to the nominal J/ψ mass [1], and the neutral *K* or hyperon candidate is constrained to originate from the J/ψ decay vertex. In addition, the fits that include the charged hyperons constrain the Λ candidate tracks to the nominal Λ mass [1], and the Ξ^- and Ω^- candidates to their respective nominal masses [1]. The Ξ^-_b and Ω^-_b mass resolutions obtained from simulated events are found to be approximately 12 MeV/c^2, a value that is comparable to the mass resolution obtained with the CDF II detector for other *b* hadrons with a J/ψ meson in the final state [12].

The selection used to reconstruct *b* hadrons is chosen to be as generally applicable as possible, in order to minimize systematic effects in rate comparisons, and to provide confidence that the observation of $\Omega^-_b \to J/\psi\Omega^-$ is not an artifact of the selection. Therefore, the final samples of all *b* hadrons used in this analysis are selected with a small number of requirements that can be applied to any *b* hadron candidate. First, *b* hadron candidates are required to have $p_T > 6.0$ GeV/c and the neutral *K* or hyperon to have $p_T > 2.0$ GeV/c. These p_T requirements restrict the sample to candidates that are within the kinematic range where our acceptance is well modeled. Mass ranges are imposed on the decay products of the *K* and hyperon candidates based on observed mass resolution or natural width, as listed in Table I. The promptly-produced combinatorial background is suppressed by rejecting candidates with low proper decay time, $t \equiv f(B)M(B)/(cp_T(B))$, where $M(B)$ is the measured mass, $p_T(B)$ is the transverse momentum, and $f(B)$ is the flight distance of the *b* hadron candidate measured with respect to the primary vertex.

Combinations that are inconsistent with having originated from the collision are rejected by imposing an upper limit on the impact distance of the *b* hadron candidate measured with respect to the primary vertex (PV) d_{PV}. Similarly, the trajectory of the decay hadron is required to originate from the *b* hadron decay vertex by imposing an upper limit on its impact distance $d_{\mu\mu}$ with respect to the vertex found in the J/ψ fit. These two impact distance quantities are compared to their measurement uncertainties $\sigma_{d_{\text{PV}}}$ and $\sigma_{d_{\mu\mu}}$ when they are used.

IV. OBSERVATION OF THE DECAY $\Omega^-_b \to J/\psi\Omega^-$

The $J/\psi\Omega^-$ mass distribution with $d_{\text{PV}} < 3\sigma_{d_{\text{PV}}}$ and $d_{\mu\mu} < 3\sigma_{d_{\mu\mu}}$ is shown in Fig. 5 for the full sample and two different requirements of *ct*. The samples with a *ct* requirement of 100 μm or greater show clear evidence of a resonance near a mass of 6.05 GeV/c^2, with a width con-
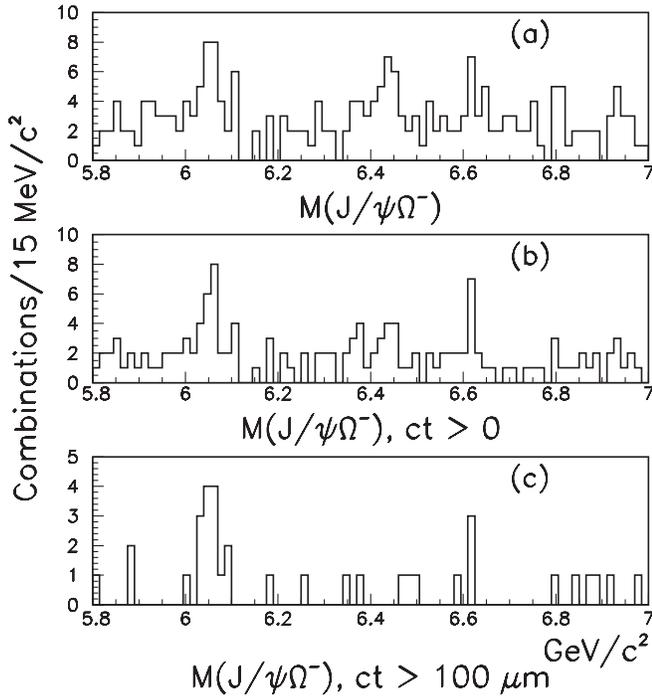
FIG. 5. (a) The mass distribution of all $J/\psi\Omega^-$ combinations. (b) The $J/\psi\Omega^-$ mass distribution for candidates with $ct > 0$. This requirement removes half of the combinations due to prompt production. (c) The $J/\psi\Omega^-$ mass distribution for candidates with $ct > 100~\mu$m. This requirement removes nearly all combinations directly produced in the $p\bar{p}$ collision.

sistent with our measurement resolution. Mass sideband regions have been defined as 8 MeV/c^2 wide ranges, centered 20 MeV/c^2 above and below the nominal Ω^- mass, as indicated in Fig. 3. The $J/\psi\Lambda K^-$ mass distribu-
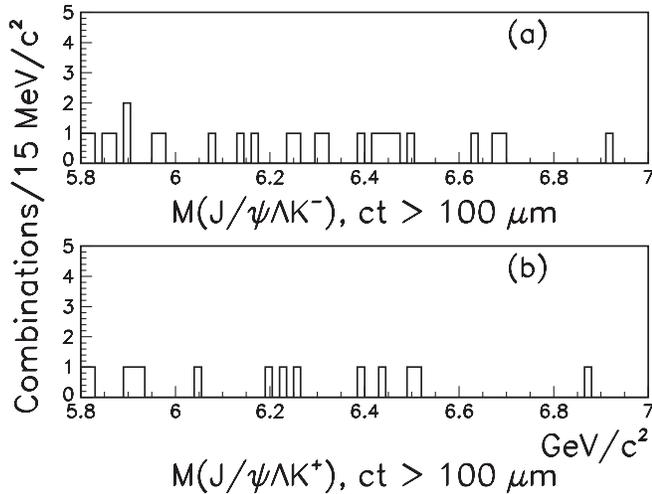
FIG. 6. (a) The invariant mass distributions of $J/\psi\Lambda K^-$ combinations for candidates with ΛK^- in the Ω^- sidebands. (b) The invariant mass distributions of $J/\psi\Lambda K^+$ combinations for candidates with ΛK^+ in the Ω^- signal range. All other selection requirements are as in Fig. 5(c).

tion for combinations that populate the Ω^- mass sideband regions is shown in Fig. 6(a). In addition, the $J/\psi\Lambda K^+$ distribution for combinations where the ΛK^+ mass populates the Ω^- signal region is shown in Fig. 6(b). No evidence of any mass resonance structure appears in either of these distributions.

The only selection criteria unique to this analysis are those used in the Ω^- selection. Therefore, the quantities used in the Ω^- selection were varied to provide confidence that the resonance structure centered at 6.05 GeV/c^2 is not peculiar to the values of the selection requirements that were chosen. The first selection criterion that was varied is the ΛK^- mass range used to define the Ω^- sample. For the candidates that satisfy the selection used in Fig. 5(c), the ΛK^- mass range was opened to ± 50 MeV/c^2. The ΛK^- mass distribution for combinations with a $J/\psi\Lambda K^-$ mass in the range 6.0–6.1 GeV/c^2 is shown in Fig. 7(a). A clear indication of an Ω^- signal can be seen, as expected for a real decay process. The ΛK^- mass range of ± 8 MeV/c^2 used in the selection was chosen to be inclusive for all likely Ω^- candidates. More restrictive mass ranges for the Ω^- selection are shown in Figs. 7(b) and 7(c), where the ΛK^- mass range is reduced to ± 6 and ± 4 MeV/c^2, respectively. The apparent excess of $J/\psi\Omega^-$ combinations
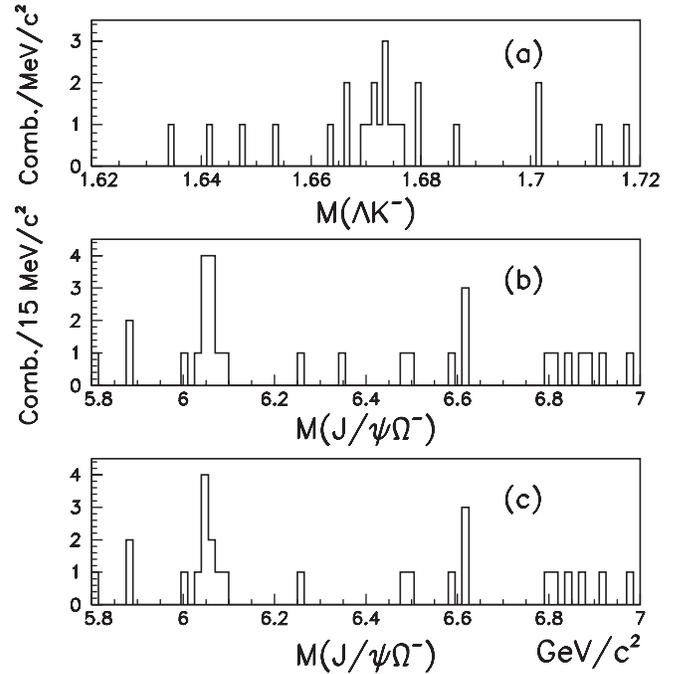

FIG. 7. (a) The invariant mass distribution of ΛK^- combinations for candidates with $J/\psi\Lambda K^-$ masses in the range 6.0–6.1 GeV/c^2. (b) The invariant mass distribution of $J/\psi\Lambda K^-$ combinations for candidates with ΛK^- masses within 6 MeV/c^2 of the Ω^- mass. (c) The invariant mass distributions of $J/\psi\Lambda K^-$ combinations for candidates with ΛK^- masses within 4 MeV/c^2 of the Ω^- mass. All other selection requirements are as in Fig. 5(c).

in the 6.0–6.1 GeV/c^2 mass range is retained for these more restrictive requirements.

A transverse flight requirement of 1 cm is used for the Ω^- selection. A lower value allows more promptly-produced background into the sample, due to our measurement resolution. A higher value reduces our acceptance, due to the decay of the Ω^-. Two variations of the flight requirement are shown in Figs. 8(a) and 8(b). No striking changes in the $J/\psi\Omega^-$ mass distribution appear for these variations. A more restrictive flight cut can also be imposed, which limits the sample to Ω^- candidates that are measured in the SVX II (inner radius is 2.5 cm), and provides the extremely pure Ω^- sample seen in Fig. 4. Two candidates in the 6.0–6.1 GeV/c^2 mass range are retained, and no others in the range expected for the Ω_b^-.

A $p_T(K^-) > 1.0$ GeV/c requirement is used in the Ω^- selection, to reduce the background due to tracks from fragmentation and other sources. The effect of three different selection values is shown in Fig. 9. The excess of $J/\psi\Omega^-$ combinations in the mass range 6.0–6.1 GeV/c^2 appears for all $p_T(K^-)$ values shown, and is probably a higher fraction of the total combinations seen for the more restrictive requirements. We conclude that the excess of $J/\psi\Omega^-$ combinations near 6.05 GeV/c^2 is not an artifact of our selection process.
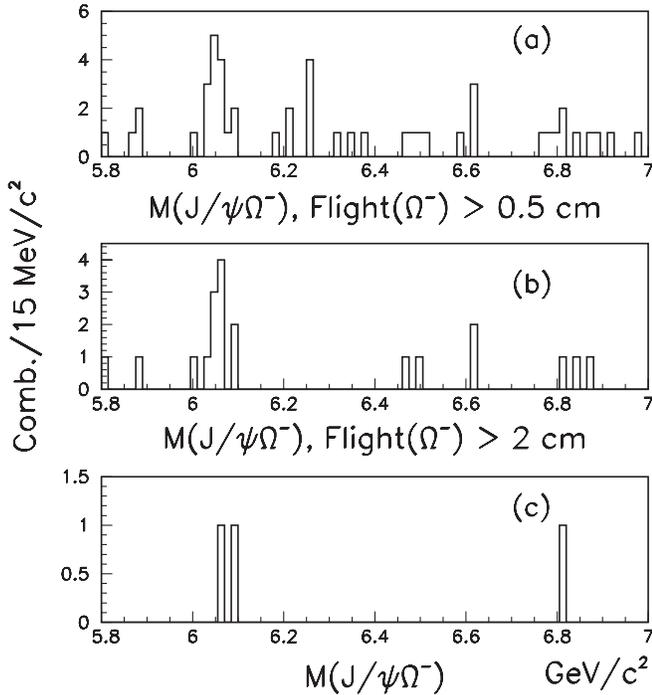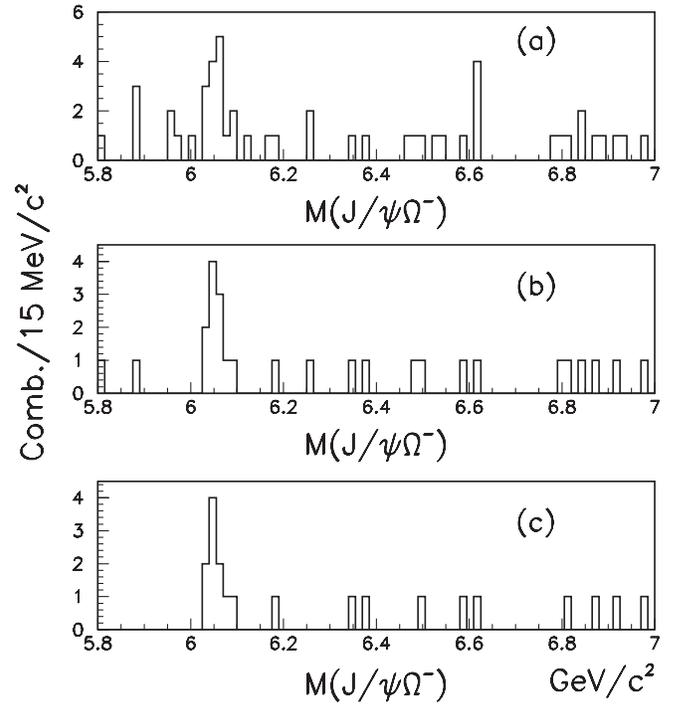

FIG. 9. The invariant mass distributions of $J/\psi\Omega^-$ combinations for candidates with three alternative requirements for the transverse momentum of the K^-. (a) $p_T(K^-) > 0.8$ GeV/c. (b) $p_T(K^-) > 1.2$ GeV/c. (c) $p_T(K^-) > 1.4$ GeV/c. All other selection requirements are as in Fig. 5(c).

The mass, yield, and significance of the resonance candidate in Fig. 5(c) are obtained by performing an unbinned likelihood fit on the mass distribution of candidates. The likelihood function that is maximized has the form

$$\mathcal{L} = \prod_i^N (f_s \mathcal{P}_i^s + (1 - f_s) \mathcal{P}_i^b)$$

$$= \prod_i^N (f_s G(m_i, m_0, s_m \sigma_i^m) + (1 - f_s) P^n(m_i)), \quad (1)$$

where N is the number of candidates in the sample, $\mathcal{P}_i^s$ and $\mathcal{P}_i^b$ are the probability distribution functions for the signal and background, respectively, $G(m_i, m_0, s_m \sigma_i^m)$ is a Gaussian distribution with average m_0 and characteristic width $s_m \sigma_i^m$ to describe the signal, m_i is the mass obtained for a single $J/\psi\Omega^-$ candidate, σ_i^m is the resolution on that mass, and $P^n(m_i)$ is a polynomial of order n. The quantities obtained from the fitting procedure include f_s, the fraction of the candidates identified as signal, m_0, the best average mass value, s_m, a scale factor on the mass resolution, and the coefficients of $P^n(m_i)$.

Two applications of this mass fit are used with the $J/\psi\Omega^-$ combinations shown in Fig. 5(c). For this data sample, all background polynomials are first order and the mass resolution is fixed to 12 MeV/c^2. The first of these fits allows the remaining parameters to vary. The second

FIG. 8. (a,b) The invariant mass distribution of $J/\psi\Omega^-$ combinations for candidates where the transverse flight requirement of the Ω^- is greater than 0.5 and 2.0 cm. (c) The invariant mass distribution of $J/\psi\Omega^-$ combinations for candidates with at least one SVX II measurement on the Ω^- track. All other selection requirements are as in Fig. 5(c).

application corresponds to the null signal hypothesis, and fixes $f_s = 0.0$, thereby removing f_s and m_0 as fitting variables. The value of $-2\ln\mathcal{L}$ for the null hypothesis exceeds the fit with variable f_s by 27.9 units for the sample with $ct > 100$ μm. We interpret this as equivalent to a χ^2 with 2 degrees of freedom (one each for f_s and m_0), whose probability of occurrence is 8.7×10^{-7}, corresponding to a 4.9σ significance. This calculation was checked by a second technique, which used a simulation to estimate the probability for a pure background sample to produce the observed signal anywhere within a 400 MeV/c^2 range. The simulation randomly distributed the number of entries in Fig. 5(c) over its mass range. Each resulting distribution was then fit with both the null hypothesis and where f_s and m_0 are allowed to vary. The simulation result, based on the distribution of $\delta(2\ln\mathcal{L})$ from 10^7 trials, confirmed the significance obtained by the ratio-of-likelihoods test.

An alternative to the mass fit obtained by maximizing Eq. (1) is to simultaneously fit mass and lifetime information. This can be accomplished by replacing the probability distribution functions used in the likelihood definition. Lifetime information for the signal term can be added by setting $\mathcal{P}_i^s = \mathcal{P}_i^{s,m}\mathcal{P}_i^{s,ct}$ where $\mathcal{P}_i^{s,m}$ is the mass distribution as in Eq. (1), and $\mathcal{P}_i^{s,ct}$ describes the distribution in ct. The background can have both prompt and b hadron decay contributions. These are included by setting $\mathcal{P}_i^b = (1 - f_B)\mathcal{P}_i^{p,m}\mathcal{P}_i^{p,ct} + f_B\mathcal{P}_i^{B,m}\mathcal{P}_i^{B,ct}$ where $\mathcal{P}_i^{p,m}$ and $\mathcal{P}_i^{p,ct}$ are the prompt mass and lifetime terms, $\mathcal{P}_i^{B,m}$ and $\mathcal{P}_i^{B,ct}$ are the b hadron decay terms, and f_B is the fraction of the background due to b hadron decay. The time distribution of the prompt background $\mathcal{P}_i^{p,ct}$ is simply due to measurement resolution and is given by $G(ct_i, 0, \sigma_i^{ct})$, where ct_i is the ct of candidate i, and σ_i^{ct} is its measurement resolution. The time probability distribution of the signal is an exponential convoluted with the measurement resolution, given by

$$\mathcal{S}(ct_i, c\tau, \sigma_i^{ct}) = \frac{1}{c\tau} \exp\left(\frac{1}{2}\left(\frac{\sigma_i^{ct}}{c\tau}\right)^2 - \frac{ct_i}{c\tau}\right)$$
$$\times \operatorname{erfc}\left(\frac{\sigma_i^{ct}}{\sqrt{2}c\tau} - \frac{ct_i}{\sqrt{2}\sigma_i^{ct}}\right), \quad (2)$$

where τ is the b hadron lifetime. A similar model is used for the b hadron decay background. Therefore, these time distributions are given by $\mathcal{P}_i^{s,ct} = \mathcal{S}(ct_i, c\tau, \sigma_i^{ct})$ and $\mathcal{P}_i^{B,ct} = \mathcal{S}(ct_i, c\tau_B, \sigma_i^{ct})$, and the new likelihood becomes

$$\mathcal{L} = \prod_i^N (f_s\mathcal{P}_i^{s,m}\mathcal{P}_i^{s,ct} + (1 - f_s)((1 - f_B)\mathcal{P}_i^{p,m}\mathcal{P}_i^{p,ct}$$
$$+ f_B\mathcal{P}_i^{B,m}\mathcal{P}_i^{B,ct})). \quad (3)$$

The simultaneous mass and lifetime likelihood in Eq. (3) is maximized for two different conditions. Both calculations use $\sigma_i^m = 12$ MeV/c, and $\sigma_i^{ct} = 30$ μm, which is the average resolution found for all other final states re-

constructed in this analysis. The first maximization allows all other parameters to vary in the fit. The second calculation fixes $f_s = 0.0$, as was done for the mass fit. The value of $-2\ln\mathcal{L}$ obtained for the null hypothesis is higher than the value obtained for the fully varying calculation by 37.3 units. We interpret this as equivalent to a χ^2 with 3 degrees of freedom, which has a probability of occurrence of 4.0×10^{-8}, or a 5.5σ fluctuation. Consequently, we interpret the $J/\psi\Omega^-$ mass distributions shown in Fig. 5 to be the observation of a weakly decaying resonance, with a width consistent with the detector resolution. We treat this resonance as observation of the Ω_b^- baryon through the decay process $\Omega_b^- \to J/\psi\Omega^-$.

V. Ξ_b^- AND Ω_b^- PROPERTY MEASUREMENTS

For the measurement of Ω_b^- properties, the impact distance requirements placed on the $J/\psi\Omega^-$ sample discussed above are not used. These requirements reduce the combinatorial background to the Ω_b^- signal, but do not have the same efficiency for other b hadrons, since the silicon detector efficiency for the charged hyperons is different for each state. Consequently, the charged hyperon helix with silicon detector measurements is not used any further. The remainder of the analysis uses silicon information only on the muons of the final states. The hadron tracks are all measured exclusively in the COT to achieve uniformity across all the b hadron states discussed in this paper.

A. Mass measurements

To reduce the background to b hadrons due to prompt production, a $ct > 100$ μm requirement is placed on all candidates for inclusion in the mass measurements. Masses are calculated by maximizing the likelihood function given in Eq. (1). The mass distributions of the candidates are shown in Figs. 10 and 11, along with projections of the fit function. The results of this fit are listed in Table II. The resolution scale factor used for the Ω_b^- fit is fixed to the value obtained from the Ξ_b^-, since the small sample size makes a scale factor calculation unreliable.

The mass difference between the B^0 as measured in the $J/\psi K_s^0$ and the nominal B^0 mass value is 0.7 MeV/c^2 [1]. This measurement is the best calibration available to establish the mass scale of the baryons measured with hyperons in the final state, because it involves a J/ψ and displaced tracks. Therefore, we use this B^0 mass discrepancy to establish the systematic uncertainty on the Ξ_b^- and Ω_b^- mass measurements. For the $B^0 \to J/\psi K_s^0$ mass measurement, approximately 3595 MeV/c^2 is taken up by the masses of the daughter particles. The remaining 1685 MeV/c^2 is measured by the tracking system. This measured mass contribution is approximately 1370 MeV/c^2 for the Ξ_b^- and 1290 MeV/c^2 for the Ω_b^-, corresponding to $\sim$80% of the B^0 value. Consequently, we
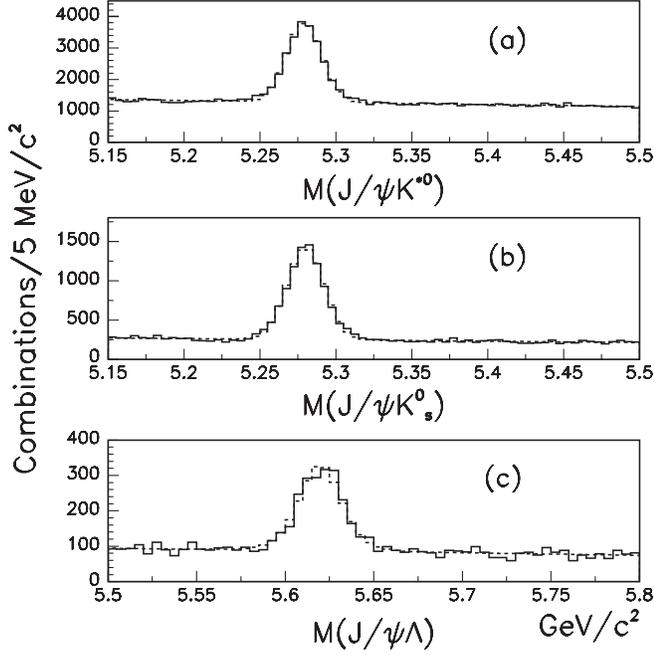
FIG. 10. The invariant mass distributions of (a) $J/\psi K^*(892)^0$, (b) $J/\psi K_s^0$, and (c) $J/\psi\Lambda$ combinations for candidates with $ct > 100\ \mu$m. The projections of the unbinned mass fits are indicated by the dashed histograms.
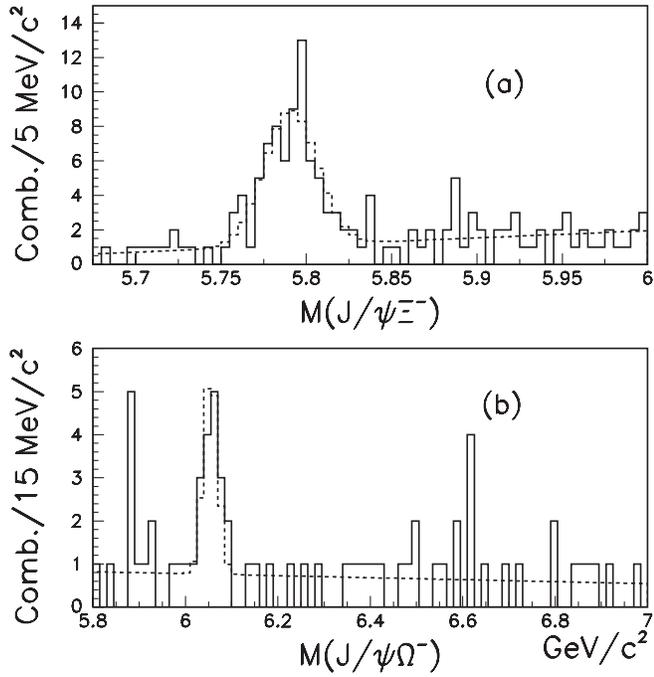

FIG. 11. The invariant mass distributions of (a) $J/\psi\Xi^-$ and (b) $J/\psi\Omega^-$ combinations for candidates with $ct > 100\ \mu$m. The projections of the unbinned mass fit are indicated by the dashed histograms.

TABLE II. Masses obtained for b hadrons.

Resonance	Candidates	Mass (MeV/c^2)	Resolution scale
$B^0(J/\psi K^*(892)^0)$	$15\,181 \pm 200$	5279.2 ± 0.2	0.98 ± 0.02
$B^0(J/\psi K_s^0)$	7424 ± 113	5280.2 ± 0.2	1.04 ± 0.02
Λ_b^0	1509 ± 58	5620.3 ± 0.5	1.04 ± 0.02
Ξ_b^-	61 ± 10	5790.9 ± 2.6	1.3 ± 0.2
Ω_b^-	12 ± 4	6054.4 ± 6.8	1.3

take this fraction of the B^0 mass measurement discrepancy to give an estimated systematic uncertainty of 0.55 MeV/c^2 for the Ξ_b^- and Ω_b^- mass scale.

A shift of 0.5 MeV/c^2 is seen in our mass measurement of the Λ_b^0, depending on whether the σ_i^m used in the fit is a constant 12 MeV/c^2 or is calculated for each event, based on the track parameter uncertainties. This effect is not statistically significant, but could appear in the Ξ_b^- and Ω_b^- mass calculations. Therefore, it is considered to be a systematic uncertainty. In addition, variations of ± 0.3 MeV/c^2 appear if the uncertainty scale factor s_m is varied over the range 1.1–1.5. Finally, the Ξ_b^- and Ω_b^- mass calculations depend on the rest masses of the decay daughters, since mass constraints are used in the candidate fit. Only uncertainty on the mass of the Ω^-, which is known to ± 0.3 MeV/c^2 [1], contributes significantly. The quadrature sum of these effects is taken to obtain the final systematic uncertainty of 0.8 MeV/c^2 for the Ξ_b^- mass measurement, and 0.9 MeV/c^2 for the Ω_b^- mass measurement. The mass of the Ξ_b^- is found to be 5790.9 ± 2.6(stat) ± 0.8(syst) MeV/c^2, which is in agreement with, and supersedes, our previous measurement [4]. The mass of the Ω_b^- is measured to be 6054.4 ± 6.8(stat) ± 0.9(syst) MeV/c^2. This value is consistent with most predictions of the Ω_b^- mass, which fall in the range 6010–6070 GeV/c^2 [2].

B. Lifetime measurements

The lifetime of b hadrons is measured in this analysis by a technique that is insensitive to the detailed lifetime characteristics of the background. This allows a lifetime calculation to be performed on a relatively small sample, since a large number of events is not needed for a background model to be developed. The data are binned in ct, and the number of signal candidates in each ct bin is compared to the value that is expected for a particle with a given lifetime and measurement resolution.

The calculation begins by expanding Eq. (1) into a form that is binned in ct. We maximize a likelihood function of the form

$$\mathcal{L} = \prod_{j=1}^{N_b} \prod_{i=1}^{N_j} [f_j G(m_i, m_0, s_m \sigma_i^m) + (1 - f_j) P_j^1(m_i)], \quad (4)$$

where N_b is the number of ct bins, N_j is the number of candidates in bin j, f_j is the signal fraction found for bin j, and $P_j^1(m_i)$ is a first order polynomial for bin j that describes the background. This fit finds a single value of mass and resolution for all the data, and provides a best estimate of the number of candidates in each ct range.

The maximization of Eq. (4) provides a fraction R_j of the total signal in ct bin j given by $R_j = f_j N_j / \sum_{i=1}^{N_b} f_i N_i$ and its measurement uncertainty σ_{R_j}. The lifetime τ can then be calculated by maximizing the likelihood function given by

$$\mathcal{L} = \prod_{j=1}^{N_b} G(R_j, w_j, \sigma_{R_j}), \qquad (5)$$

where w_j is the fraction of the signal that is calculated to occupy bin j. The measured lifetime distribution of b hadrons is a resolution-smeared exponential, given by Eq. (2). The expected content of each ct bin is then given by $w_j = \int_{ct_{\text{low}}^j}^{ct_{\text{high}}^j} \mathcal{S}((ct), c\tau, \sigma^{(ct)}) d(ct)$, where ct_{high}^j and ct_{low}^j are the boundaries of ct bin j.

In this application of the lifetime calculation, five bins in ct were used for all samples except the Ω_b^-, where the small sample size motivated the use of four bins. Studies with the B^0 sample indicate that little additional precision is gained by using more than five ct bins. The bin boundary between the lowest two bins was chosen to be $ct_{\text{high}}^1 = 100~\mu$m. This choice has the effect of placing the largest fraction of the combinatorial background into the first bin. The remaining bin boundaries were chosen to place an equal number of candidates into each remaining bin, assuming they follow an exponential distribution with a characteristic lifetime given by the initial value, $c\tau_{\text{init}}$, chosen for the fit. This algorithm gives the lower bin edges for the second and subsequent bins at $ct_{\text{low}}^j = ct_{\text{high}}^1 - c\tau_{\text{init}} \ln(\frac{N_b-j}{N_b-1})$. The lowest (highest) bin is unbounded on the low (high) side.

All final states used in this analysis have three or more SVX II hits on each muon track, but not on any of the other tracks in the reconstruction. This provides a comparable ct resolution across the final states, which falls in the range $15~\mu$m $< \sigma_i^{ct} < 40~\mu$m. The average value of σ_i^{ct} obtained from the B^0 and Λ_b^0 candidates is $30~\mu$m, and this value was used in the lifetime fits. The signal yields and lifetimes obtained by maximizing Eq. (5) appear in Table III along with the statistical uncertainties on these quantities. Comparisons between the number of candidates in each ct bin and the fit values are shown in Figs. 12 and 13. The fits for the B^0 and Λ_b^0 were repeated for a variety of different σ_i^{ct} over the range from 0 to $60~\mu$m. The resulting value of $c\tau$ varied by $\pm 2~\mu$m, which is taken as a systematic uncertainty due to the treatment of σ_i^{ct}. The B^0 and Λ_b^0 $c\tau$ varied by $\pm 5~\mu$m for different choices of N_b, so this is

TABLE III. Signal yields and lifetimes obtained for the b hadrons.

Resonance	Yield	$c\tau$ (μm)
$B^0(J/\psi K^*(892)^0)$	$17\,250 \pm 305$	453 ± 6
$B^0(J/\psi K_s^0)$	9424 ± 167	448 ± 7
Λ_b^0	1934 ± 93	472 ± 17
Ξ_b^-	66_{-9}^{+14}	468_{-74}^{+82}
Ω_b^-	16_{-4}^{+6}	340_{-120}^{+160}

considered an additional possible systematic uncertainty. No systematic effect has been seen due to the choice of $c\tau_{\text{init}}$, which was chosen to be $475~\mu$m for the B^0, Λ_b^0 and Ξ_b^-, and $250~\mu$m for the Ω_b^-. Systematic effects due to the detector misalignment are estimated not to exceed $1~\mu$m. The estimates of these effects, combined in quadrature, provide a systematic uncertainty of $6~\mu$m on the B^0 lifetime measurements, a relative uncertainty of 1.3%. The results of the B^0 lifetime measurements are consistent with the nominal value of $459 \pm 6~\mu$m [1], which serves as a check on the analysis technique. In addition, the lifetime result obtained here for the Λ_b^0 is consistent with our previous measurement [13], which was based on a continuous lifetime fit similar to Eq. (3). Consequently, a systematic uncertainty of 1.3% of the central lifetime value
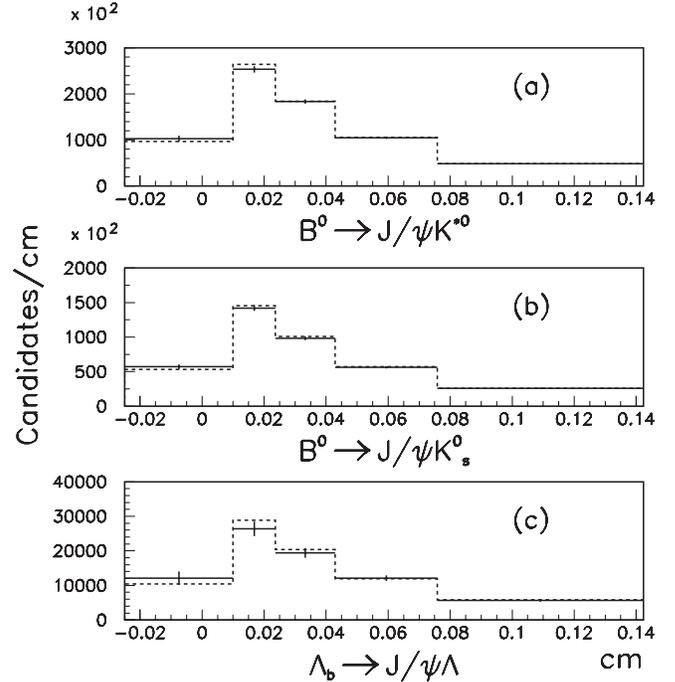

FIG. 12. The solid histograms represent the number of (a) $B^0 \to J/\psi K^*(892)^0$, (b) $B^0 \to J/\psi K_s^0$, and (c) $\Lambda_b \to J/\psi \Lambda$ candidates found in each ct bin. The dashed histogram is the fit value. Yields and fit values are normalized to candidates per cm, and the bin edges are indicated. The highest and lowest bins are not bounded, but are truncated here for display purposes.
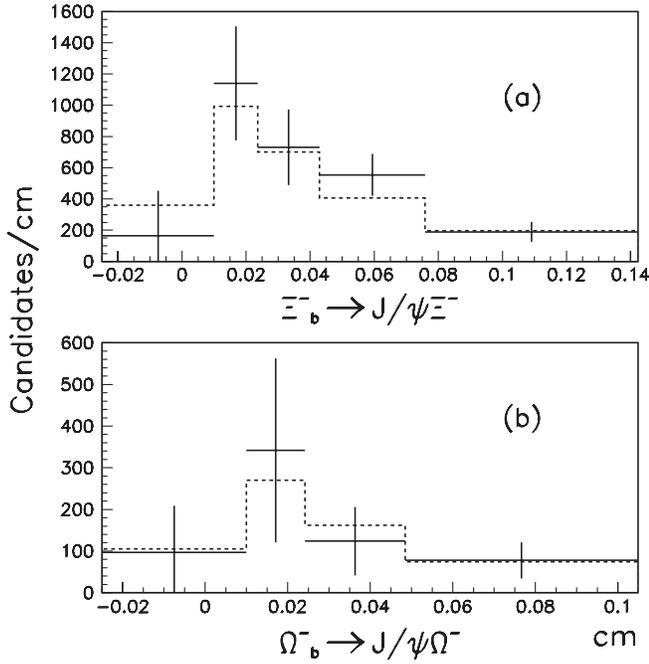
FIG. 13. The solid histograms represent the number of (a) $\Xi_b^- \to J/\psi\,\Xi^-$ and (b) $\Omega_b^- \to J/\psi\,\Omega^-$ candidates found in each ct bin. The dashed histogram is the fit value. Yields and fit values are normalized to candidates per cm, and the bin edges are indicated. The highest and lowest bins are not bounded, but are truncated here for display purposes.

is taken for the b baryon lifetime measurements. We measure the lifetime of the Ξ_b^- to be $1.56^{+0.27}_{-0.25}(\text{stat}) \pm 0.02(\text{syst})$ ps and the lifetime of the Ω_b^- to be $1.13^{+0.53}_{-0.40}(\text{stat}) \pm 0.02(\text{syst})$ ps.

C. Relative production rate measurements

A further goal of this analysis is to measure the production rates of the Ξ_b^- and Ω_b^-, relative to the more plentiful Λ_b^0, where we measure ratios of cross sections times branching fractions. In the case of the Ξ_b^-, we evaluate

$$
\frac{\sigma(\Xi_b^-)\mathcal{B}(\Xi_b^- \to J/\psi\,\Xi^-)\mathcal{B}(\Xi^- \to \Lambda\pi^-)}{\sigma(\Lambda_b^0)\mathcal{B}(\Lambda_b^0 \to J/\psi\,\Lambda)}
$$
$$
= \frac{N_{\text{data}}(\Xi_b^- \to J/\psi\,\Xi^-)}{N_{\text{data}}(\Lambda_b^0 \to J/\psi\,\Lambda)} \frac{\epsilon_{\Lambda_b^0}}{\epsilon_{\Xi_b^-}}, \tag{6}
$$

where $\sigma(h)$ is the production cross section of hadron h, $\mathcal{B}$ corresponds to the indicated branching fractions, N_{data} are the number of indicated candidates seen in the data, and ϵ_h is the acceptance and reconstruction efficiency for hadron h. A similar expression for the Ω_b^- applies as well.

The hyperon branching fractions are well measured, and we use the nominal values for these quantities [1]. The number of events for each state is obtained from the lifetime fit technique described previously (Sec. V B) and listed in Table III. The acceptance and efficiency terms

require careful consideration because the acceptance of the CDF tracking system is not well modeled for tracks with $p_T < 400$ MeV/c. Consequently, the calculation of total acceptance is dependent on the assumed p_T distribution of the particle of interest. Simple application of our simulation to estimate the total efficiency would leave the results with a dependence on the underlying generation model [8], which is difficult to estimate. Therefore, a strategy has been adopted to reduce the sensitivity of the relative rate measurement to the simulation assumptions. This method divides the data into subsets, defined by limited ranges of p_T. The efficiency over a limited range of p_T can be calculated more reliably, since the variation of a reasonable simulation model, such as the one used here, is small over the limited p_T range.

As was done with the mass and lifetime measurements, the B^0 sample is used as a reference point for the relative rate measurement. In analogy to Eq. (6), the ratio of branching fractions for the B^0 is given by

$$
\frac{\mathcal{B}(B^0 \to J/\psi\,K^0)\mathcal{B}(K^0 \to K_s^0)\mathcal{B}(K_s^0 \to \pi^+\pi^-)}{\mathcal{B}(B^0 \to J/\psi\,K^*(892)^0)\mathcal{B}(K^*(892)^0 \to K^+\pi^-)}
$$
$$
= \frac{N_{\text{data}}(B^0 \to J/\psi\,K_s^0)}{N_{\text{data}}(B^0 \to J/\psi\,K^*(892)^0)} \frac{\epsilon_{K^*(892)^0}}{\epsilon_{K_s^0}}. \tag{7}
$$

The branching fractions are taken to be $\mathcal{B}(K^0 \to K_s^0) = 0.5$, $\mathcal{B}(K^*(892)^0 \to K^+\pi^-) = 2/3$, and $\mathcal{B}(K_s^0 \to \pi^+\pi^-) = 0.692$ [1]. The number of candidates for each final state obtained for several p_T ranges is then combined with the acceptance and reconstruction efficiency for that range to obtain the ratio of branching fractions indicated in Table IV. The full range of 6–20 GeV/c was chosen to correspond to the range of data available in the Ξ_b^- and Ω_b^- samples. These results are consistent with the nominal value of 0.655 ± 0.038 [1] for the branching fraction ratio, and provide confirmation of the accuracy of the detector simulation for these states.

The samples of Ξ_b^- and Ω_b^- are too small to be divided into ranges of p_T, as is done for the B^0. Therefore, the acceptance and reconstruction efficiency must be obtained over the wider range of 6–20 GeV/c, and a production distribution as a function of p_T must be assumed over this range. The production distribution used here is derived from the data, rather than adopting a theoretically motivated model. The derivation assumes that the Ξ_b^- and Ω_b^- are produced with the same p_T distribution as the Λ_b^0. We then use the observed p_T distribution of Λ_b^0 production to obtain the total efficiency for the Ξ_b^- and Ω_b^- states.

The first step in obtaining the total acceptance and reconstruction efficiency terms is to divide the Λ_b^0 sample into several ranges of p_T. The number of candidates is found by fitting each sample with the likelihood defined in Eq. (1). The reconstruction efficiency for the Λ_b^0 in each range of p_T was obtained by simulating events through the full detector simulation. The yield and efficiency are then

TABLE IV. The yields of B^0 candidates obtained for several ranges of $p_T(B^0)$ and the branching fraction ratio obtained for each subset.

p_T (GeV/c)	$B^0 \to J/\psi K^*(892)^0$	$B^0 \to J/\psi K_s^0$	$\frac{\mathcal{B}(B^0 \to J/\psi K^0)}{\mathcal{B}(B^0 \to J/\psi K^*(892)^0)}$
6–7.5	2640 ± 74	1196 ± 23	0.59 ± 0.04
7.5–9	2687 ± 52	1361 ± 50	0.64 ± 0.03
9–11	3189 ± 49	1685 ± 34	0.63 ± 0.03
11–14	3243 ± 54	1615 ± 50	0.64 ± 0.03
14–20	2787 ± 56	1321 ± 27	0.63 ± 0.03
6–20	$14\,546 \pm 129$	7178 ± 98	0.628 ± 0.014

TABLE V. The efficiencies of Ξ_b and Ω_b candidates obtained for several ranges of p_T and the fraction of Λ_b^0 events produced for each range. For the total efficiency over the p_T range 6–20 GeV/c^2, the first uncertainty term is due to the Λ_b^0 sample, and the second is due to the simulation sample size.

p_T (GeV/c)	$f_j^{\Lambda_b^0}$	$\epsilon_{\Lambda_b^0}(p_T) \times 10^{-2}$	$\epsilon_{\Xi_b}(p_T) \times 10^{-3}$	$\epsilon_{\Omega_b}(p_T) \times 10^{-3}$
6–7.5	0.411 ± 0.031	1.40 ± 0.04	2.37 ± 0.14	2.21 ± 0.17
7.5–9	0.277 ± 0.020	2.59 ± 0.06	4.96 ± 0.28	6.73 ± 0.41
9–11	0.168 ± 0.011	4.14 ± 0.10	9.40 ± 0.44	11.54 ± 0.61
11–14	0.092 ± 0.006	6.39 ± 0.14	16.08 ± 0.71	23.26 ± 1.02
14–20	0.052 ± 0.005	9.32 ± 0.22	24.19 ± 1.11	40.27 ± 1.96
6–20		$3.07 \pm 0.14 \pm 0.04$	$6.67 \pm 0.22 \pm 0.17$	$8.96 \pm 0.32 \pm 0.24$

combined to give a quantity that is proportional to $\sigma(\Lambda_b^0)\mathcal{B}(\Lambda_b^0 \to J/\psi \Lambda)$ for each range of p_T. The acceptance and reconstruction efficiency terms for each p_T range, $\epsilon_{\Xi_b}(p_T)_j$, are simply obtained from the simulation. The total reconstruction efficiency over the full range of p_T is $\epsilon_{\Xi_b} = \sum_j^{N_j} f_j^{\Lambda_b^0} \epsilon_{\Xi_b}(p_T)_j$ where N_j is the number of p_T ranges, and $f_j^{\Lambda_b^0}$ is the fraction of the Λ_b^0 produced in p_T range j. These factors and their statistical uncertainties appear in Table V. The p_T integrated acceptance and efficiency terms are then used to solve Eq. (6) for the relative rates of production. The Λ_b^0 yield in the p_T range of 6–20 GeV/c is 1812 ± 61, while 66^{+16}_{-9} and 16^{+6}_{-4} are found for the Ξ_b^- and Ω_b^-, respectively. The relative production ratios are $0.167^{+0.037}_{-0.025}$ for the Ξ_b^- and $0.045^{+0.017}_{-0.012}$ for the Ω_b^- where these uncertainties are statistical, and contain the contributions from the Λ_b^0 measurements.

The total uncertainty on the efficiency contains contributions from both the calculation of $f_j^{\Lambda_b^0}$ and the size of the sample used for the simulation. These contributions were added, to obtain a total relative uncertainty on the efficiency terms of 6%. The simulation of the tracking system is accurate to within 3% for the five-track final states used in this analysis [14]. An additional 0.3% is assigned to the Ω^-, due to our characterization of the material in the detector and its effect on the K^- tracking efficiency. The uncertainty on the Ξ^- branching fraction does not contribute significantly, and the Ω^- branching fraction is known to within 1%. The mass of the Ω_b^- used in the simulation

was varied over the range 6.0–6.19 GeV/c^2, and the efficiency calculations were repeated. The efficiency was found to remain constant to within 5%. We assign this value as an additional systematic uncertainty on the Ω_b^- efficiency. An additional systematic uncertainty of 2.5% due to the Λ_b^0 yield is obtained by varying $c\tau(\Lambda_b^0)$ over a ± 50 μm range. These systematic effects were combined in quadrature to provide an estimate for the total relative systematic uncertainty on the production ratios of 7% for the Ξ_b^- and 9% for the Ω_b^-. Our measurements of the relative production rates are $\frac{\sigma(\Xi_b^-)\mathcal{B}(\Xi_b^- \to J/\psi \Xi^-)}{\sigma(\Lambda_b^0)\mathcal{B}(\Lambda_b^0 \to J/\psi \Lambda)} = 0.167^{+0.037}_{-0.025}$(stat) ± 0.012(syst) and $\frac{\sigma(\Omega_b^-)\mathcal{B}(\Omega_b^- \to J/\psi \Omega^-)}{\sigma(\Lambda_b^0)\mathcal{B}(\Lambda_b^0 \to J/\psi \Lambda)} = 0.045^{+0.017}_{-0.012}$(stat) ± 0.004(syst) for the Ξ_b^- and Ω_b^-, respectively.

VI. CONCLUSIONS

In conclusion, we have used data collected with the CDF II detector at the Tevatron to observe the Ω_b^- in $p\bar{p}$ collisions. The reconstruction used for this observation and the techniques for measuring the properties of the Ω_b^- are used on other b hadron properties that have been measured previously, which provide a precise calibration for the analysis. A signal of 16^{+6}_{-4} Ω_b^- candidates, with a significance equivalent to 5.5σ when combining both mass and lifetime information, is seen in the decay channel $\Omega_b^- \to J/\psi \Omega^-$ with $J/\psi \to \mu^+ \mu^-$, $\Omega^- \to \Lambda \pi^-$, and $\Lambda \to p\pi^-$. The mass of this baryon is measured to be 6054.4 ± 6.8(stat) ± 0.9(syst) MeV/c^2, which is consistent with

theoretical expectations [2]. In addition, we measure the lifetime of the Ω_b^- to be $1.13^{+0.53}_{-0.40}$(stat) $\pm$ 0.02(syst) ps, and the Ω_b^- production relative to the Λ_b^0 to be $\frac{\sigma(\Omega_b^-)\mathcal{B}(\Omega_b^-\to J/\psi\Omega^-)}{\sigma(\Lambda_b^0)\mathcal{B}(\Lambda_b^0\to J/\psi\Lambda)} = 0.045^{+0.017}_{-0.012}$(stat) $\pm$ 0.004(syst). The additional data available to this analysis allows an update to our previous Ξ_b^- mass measurement [4]. A new value of 5790.9 ± 2.6(stat) ± 0.8(syst) MeV/c^2 is obtained for the Ξ_b^- mass. The lifetime of the Ξ_b^- is measured to be $1.56^{+0.27}_{-0.25}$(stat) $\pm$ 0.02(syst) ps, which is the first measurement of this quantity in a fully reconstructed final state. Finally, the relative production of the Ξ_b^- compared to the Λ_b^0 is found to be $\frac{\sigma(\Xi_b^-)\mathcal{B}(\Xi_b^-\to J/\psi\Xi^-)}{\sigma(\Lambda_b^0)\mathcal{B}(\Lambda_b^0\to J/\psi\Lambda)} = 0.167^{+0.037}_{-0.025}$(stat) $\pm$ 0.012(syst).

The first reported observation of the Ω_b^- measured a mass of 6165 ± 10(stat) ± 13(syst) MeV/c^2 [6]. The mass measurement presented here differs from Ref. [6] by 111 ± 12(stat) ± 14(syst) MeV/c^2, where we have combined the statistical uncertainties of the two measurements in quadrature, and summed the systematic uncertainties. The two measurements appear to be inconsistent.

The relative rate measurement presented in Ref. [6] is $\frac{f(b\to\Omega_b^-)\mathcal{B}(\Omega_b^-\to J/\psi\Omega^-)}{f(b\to\Xi_b^-)\mathcal{B}(\Xi_b^-\to J/\psi\Xi^-)} = 0.80 \pm 0.32$(stat)$^{+0.14}_{-0.22}$(syst) where $f(b\to\Omega_b^-)$ and $f(b\to\Xi_b^-)$ are the fractions of b quarks that hadronize to Ω_b^- and Ξ_b^-. The equivalent quantity taken from the present analysis is $\frac{\sigma(\Omega_b^-)\mathcal{B}(\Omega_b^-\to J/\psi\Omega^-)}{\sigma(\Xi_b^-)\mathcal{B}(\Xi_b^-\to J/\psi\Xi^-)} = 0.27 \pm 0.12$(stat) ± 0.01(syst). Neither measurement is

very precise, since a ratio is taken of two small samples. Nevertheless, this analysis indicates a rate of Ω_b^- production substantially lower than Ref. [6]. Consequently, the analysis presented here is not able to confirm the Ω_b^- observation reported in Ref. [6]. Future work is needed to resolve the discrepancy between the two results.

[1] C. Amsler *et al.* (Particle Data Group), Phys. Lett. B **667**, 1 (2008).

[2] E. Jenkins, Phys. Rev. D **77**, 034012 (2008); R. Lewis and R. M. Woloshyn, *ibid.* **79**, 014502 (2009); D. Ebert, R. N. Faustov, and V. O. Galkin, *ibid.* **72**, 034026 (2005); M. Karliner, B. Keren-Zur, H. J. Lipkin, and J. L. Rosner, Ann. Phys. (N.Y.) **324**, 2 (2009); A. Valcarce, H. Garcilazo, and J. Vijande, Eur. Phys. J. A **37**, 217 (2008).

[3] V. M. Abazov *et al.* (D0 Collaboration), Phys. Rev. Lett. **99**, 052001 (2007).

[4] T. Aaltonen *et al.* (CDF Collaboration), Phys. Rev. Lett. **99**, 052002 (2007).

[5] T. Aaltonen *et al.* (CDF Collaboration), Phys. Rev. Lett. **99**, 202001 (2007).

[6] V. M. Abazov *et al.* (D0 Collaboration), Phys. Rev. Lett. **101**, 232002 (2008).

[7] D. Acosta *et al.* (CDF Collaboration), Phys. Rev. D **71**, 032001 (2005); A. Sill *et al.*, Nucl. Instrum. Methods Phys. Res., Sect. A **447**, 1 (2000); F. Abe *et al.* (CDF Collaboration), Phys. Rev. D **50**, 2966 (1994).

[8] P. Nason, S. Dawson, and R. K. Ellis, Nucl. Phys. **B303**, 607 (1988); **B327**, 49 (1989).

[9] C. Peterson, D. Schlatter, I. Schmitt, and P. M. Zerwas, Phys. Rev. D **27**, 105 (1983).

[10] D. J. Lange, Nucl. Instrum. Methods Phys. Res., Sect. A **462**, 152 (2001).

[11] R. Brun, R. Hagelberg, M. Hansroul, and J. C. Lassalle, CERN Reports No. CERN-DD-78-2-REV and No. CERN-DD-78-2.

[12] D. Acosta *et al.* (CDF Collaboration), Phys. Rev. Lett. **96**, 202001 (2006).

[13] A. Abulencia *et al.* (CDF Collaboration), Phys. Rev. Lett. **98**, 122001 (2007).

[14] A. Abulencia *et al.* (CDF Collaboration), Phys. Rev. D **75**, 012010 (2007).